Supporting Information

Enami *et al.* 10.1073/pnas.0710791105

SI Text

Aqueous solutions are pumped (50 μl min^{-1}; Harvard Apparatus) into the spraying chamber of a commercial ESMS instrument (HP-1100 MSD; Agilent) through a grounded stainless steel needle injector (100-μm internal diameter, 150-μm external diameter) and pneumatically nebulized by means of N_2 gas flowing through a coaxial sheath (1). The difference between the exit velocities of the liquid jet (10.6 cm s^{-1}) and nebulizer gas (2.65×10^4 cm s^{-1}) is so large that the drag imposed on the liquid breaks it apart into submicron-size droplets. The terminal velocities of the microdroplets thus produced exceed $\approx 10^3$ cm s^{-1} (2) that lead to transit times shorter than $\tau \approx 1$ ms across the $\approx$ 0.5-cm-wide O_3(g) plume. These droplets, which are produced by fragmentation of electrically neutral solutions from a grounded injector, are charged via statistical fluctuations that scale with (drop size)$^{-1/2}$ (3). The ensemble of spray droplets is, on average, neutral, but individual droplets actually carry charges that follow a Gaussian distribution, as expected for a random process. This phenomenon is the basis of the classical oil drop experiment performed by Millikan (4) to determine the magnitude of the elementary charge. It should be emphasized that spontaneous, asymmetrical charge separation during pneumatic nebulization of liquids does not produce highly charged droplets, and, therefore, it is unrelated to electrospray ionization of droplets issuing from high-field nozzles. Sprayed droplets eventually contract via solvent evaporation, a process regulated by ambient temperature and relative humidity, thereby increasing electrostatic repulsion among excess surface charges. Coulomb explosions ensue in which drops shed interfacial charge and mass into smaller droplets. In the final stage, ions are ejected from nanodroplets into the gas phase (5–7). It is apparent that, by its very nature, this technique effectively samples the interfacial layers of nanodroplets. Product identities were confirmed via MS–MS analyses performed in an Agilent MSD-Trap mass spectrometer.

Ozone is generated by flowing ultrapure O_2(g) (Air Liquid America Co.) through a commercial ozonizer (Ozone Solutions), diluted tenfold with ultrapure N_2(g), and quantified by UV absorption spectrophotometry (HP 8452) at 250 and 300 nm before entering the spraying chamber, where it contacts the aqueous AH_2 droplets for $\approx$1 ms. This arrangement has been described and illustrated in detail in ref. 1. Throughout, the reported [O_3(g)] values, which correspond to the concentrations actually sensed by microdroplets in the reaction chamber, are estimated to be $\approx$10 times smaller than the values determined from UV absorbances because of further dilution by the N_2 drying gas. Gas flows were regulated by calibrated mass flow controllers (MKS). Typical instrumental parameters were as follows: drying gas temperature, 250°C; nebulizer pressure, 2 atm; collector capillary voltage, +3.5 kV; fragmentor voltage, 17 V. We have evidence that droplets are weakly charged under present conditions. Solutions were prepared in MilliQ water, or in D_2O (D >99.9%; Cambridge Isotope Laboratories) that had been previously purged with ultrapure N_2(g) longer than 30 min. L-[$^{12}C_6$]AH_2 (> 99%; Sigma–Aldrich), L-[1-^{13}C], L-[2-^{13}C], and L-[3-^{13}C] AH_2 (Omicron), calcium threonate (Sigma–Aldrich), DHA (Sigma–Aldrich), and *tert-butanol* (Fisher) were used as received. Solutions pH was measured with a calibrated pH meter (VWR).

Appendix 1. Reactant diffusion from the droplets core may account for the leveling off, i.e., the weaker than exponential decay of [AH^-]/[AH^-]$_0$ vs. [O_3(g)] (Fig. S5 *Upper*). If the concentration of $X \equiv AH^-$ in the interfacial layers is determined by its reaction with O_3(aq) $\rightleftarrows$ O_3(g), and by diffusion from the droplets core, then:

$$\frac{\partial[X]}{\partial t} = \frac{D[X]_0 - [X]}{\delta \quad \Delta} - k[O_3][X];\ D' = \frac{D}{\delta\Delta} \qquad [1]$$

$$[X] = \frac{D'[X]_0 - k[O_3][X]_0 \exp[-(D' + k[O_3])t]}{D' + k[O_3]} \qquad [2]$$

$$\frac{[X]_{ss}}{[X]_0} = \frac{D'}{D' + k[O_3]} \qquad [3]$$

$$\frac{\partial([X]_{ss}/[X]_0)}{\partial[O_3]} \rightarrow -\frac{k}{D'} \text{ as } [O_3] \rightarrow 0 \qquad [4]$$

where D is the diffusion coefficient of X in water, δ is the thickness of the interfacial shell, and Δ is the length over which its intradroplet concentration gradient is established. k is the local (X + O_3) reaction rate constant in the interfacial layers. The solution of Eq. **1** is given by Eq. **2**. In the absence of diffusion, i.e., $D' = 0$, [X] decays exponentially with time, at constant [O_3]. However, since X can diffuse (with $D \approx 2 \times 10^{-5}$ cm^2 s^{-1}) in tens of nanoseconds through, say, a $\Delta \approx$ 10-nm layer, a stationary state should be rapidly established within the $\approx$1-ms timeframe of our experiments. This condition is encoded by equation Eq. **3**, the limiting form of Eq. **2** at $t \rightarrow \infty$. By assuming, as a first approximation, that D' is constant, the $[X]_{ss}/[X]_0$ ratio becomes an inverse rational function of [O_3] at constant contact time. The initial slope, given by Eq. **4**, is therefore proportional to the reaction rate constant k. Plots calculated from Eq. **3** for various parameter combinations (Fig. S3) show that $[X]_{ss}/[X]_0$ indeed "levels off" at large [O_3(g)], supporting our interpretation of this phenomenon. A more realistic analysis should deal with the development of intradroplet concentration gradients as functions of time, radius, and [O_3(g)] (8), but it is doubtful that classical continuum diffusion models will be adequate for this task. The leveling off of experimental [AH^-]/[AH^-]$_0$ vs. [O_3(g)] curves cannot be due to diffusional limitations in the gas-phase because this event is not replicated in the ozonolysis of other anions, such as $S_2O_3^-$ or I^-, over the same [O_3(g)] ranges in 1 atm N_2(g) (1). Note that, since intradroplet diffusion contributes significantly to monitored interfacial [X] concentrations, interfacial layers behave as open reactors in which formal product P yields calculated as: $Y_P = ([P]_f - [P]_0)/([X]_0 - [X]_f)$ may exceed unity (1, 9). Conventional integrated kinetic equations for closed, well mixed chemical reactors are, of course, inapplicable to interfacial layers.

Appendix 2. In *Appendix 1*, it was shown that the slopes of [AH^-]/[AH^-]$_0$ vs. [O_3(g)] curves at [O_3(g)] $\rightarrow$ 0 are proportional to reaction rate constants k (Eq. **4**). To obtain limiting slopes, γ, Eq. **7**, from experimental data, [AH^-]/[AH^-]$_0$ curves were fitted over the full [O_3(g)] range (Fig. S5 *Upper*) using the four-parameter expression Eq. **5**:

$$y = y_0 + a\exp(-bx) + cx \qquad [5]$$

$$y \equiv [AH^-]/[AH^-]_0;\ x \equiv [O_3(g)] \qquad [6]$$

$$\gamma = \left[\frac{\partial y}{\partial x}\right]_{x \rightarrow 0} = -ab + c \qquad [7]$$

Regression results are shown in Table S1. Notice that c values make negligible contributions to γ. γ is in [ppm^{-1}]. A γ vs. pH plot is shown in Fig. S4.

$$\gamma = \gamma_0 + \frac{A}{1 + \exp\left[\frac{pH - pH_{0.5}}{B}\right]} \quad [8]$$

$$\gamma_0 = 0.41; A = -0.26; B = 0.21; pH_{0.5} = 3.98$$

Appendix 3. Initial slopes in Fig. 3:

$$\gamma_P = \left[\frac{\partial[P]}{\partial[O_3]}\right]_{[O_3]\to 0} (P \equiv \text{DHA, THR, or AOZ}) \quad [9]$$

were calculated from best-fit numerical regressions to experimental data. Second-order polynomials ($[P] = A_0 + A_1[O_3(g)] + A_2[O_3(g)]^2$; $\gamma_P = A_1$) were used in the case of $P \equiv$ THR and AOZ, and exponential growth curves ($[P] = B_0 + B_1 \times\{1 - \exp(-B_2[O_3(g)])\}$; $\gamma_P = B_1 \times B_2$) for $P \equiv$ DHA, <20 ppm [O_3(g)]. Concentrations are directly proportional to signal intensities in these ranges. The results are shown in Table S2. γ_P is in [signal intensity/a.u. ppm^{-1}]. The ($\gamma_{THR}/\gamma_{DHA}$)and($\gamma_{AOZ}/\gamma_{DHA}$) ratios are plotted as function of pH in Fig. 4*a*. The ratios of the corresponding signal intensities measured at 800 ppm [O_3(g)] as functions of pH, which are more representative of net product formation after the complete decomposition of the primary ozonide intermediate POZ, are shown in Fig. 4*b*.

Appendix 4. The dissimilar evolution of AH_2 and DHA versus THR and AOZ with [O_3(g)] indicate that DHA is a primary product, whereas THR and AOZ ensue from the decomposition of an unstable intermediate, probably the primary ozonide POZ (Scheme 1). A $\equiv$ [AH_2], B $\equiv$ [DHA], C $\equiv$ [POZ] and D $\equiv$ [AOZ]; [AH^-] = α [AH_2] throughout. The following simplified mechanism should describe our system at small conversions, i.e., barring extensive diffusion (see Appendix 1):

$A + O_3 \to B$; $\alpha k_1 = k_1'$
$A + O_3 \to C$; $(1 - \alpha)k_2 = k_2'$
$C \to D$; k_3
$C + O_3 \to D$; k_4
$f = \exp(-(k_1' + k_2')[O_3]t)$
$g = \exp(-(k_3 + k_4)[O_3]t)$
$h = k_2'[O_3]/(k_3 + (k_4 - k_1' - k_2')[O_3])$
$m = k_1'/(k_1' + k_2')$
$A_0 = 1$; $B_0 = C_0 = D_0 = 0$
$B = m(1 - f)$; $C = h(f - g)$; $D = 1 - f - m(1 - f) - h(f - g)$

Fig. S7 shows experimental data for DHA and AOZ vs. [O_3(g)] at pH 5.8 (from Fig. 3) and the results of evaluating B and D using $\tau = 0.001$ s, $k_1' = 600$, $k_2' = 200$, $k_4 = 12$ (in $ppm^{-1}\,s^{-1}$ units) and $k_3 = 50\ s^{-1}$, in the equations above. The dashed line corresponds to the curve calculated by substituting ($k_3 = 0$; $k_4 = 16\ ppm^{-1}\ s^{-1}$) for ($k_3 = 50\ s^{-1}$; $k_4 = 12\ ppm^{-1}\ s^{-1}$) in the previous set of parameters. It is apparent that the decomposition of POZ involves unimolecular (step 3) and ozone-catalyzed (step 4) pathways (10). Neither pathway alone is able to account for a nonvanishing initial slope γ_{AOZ} and increased AOZ production at larger [O_3(g)]. At the [O_3(g)] <0.5 ppm concentrations prevalent in polluted atmospheres, the decomposition of POZ will largely proceed unimolecularly via step 3 in less than ≈1 s.

1. Enami S, Vecitis CD, Cheng J, Hoffmann MR Colussi AJ (2007) Electrospray mass spectrometric detection of products and short-lived intermediates in aqueous aerosol microdroplets exposed to a reactive gas. *J Phys Chem A* 111:13032–13037.
2. Kahen K, Jorabchi K, Gray C, Montaser A (2004) Spatial mapping of droplet velocity and size for direct and indirect nebulization in plasma spectrometry. *Anal Chem* 76:7194–7201.
3. Dodd EE (1953) The statistics of liquid spray and dust electrification by the hopper and laby method. *J Appl Phys* 24:73–80.
4. Millikan RA (1910) The isolation of an ion, a precision measurement of its charge, and the correction of Stokes's law. *Science* 32:436–448.
5. Fenn JB (1993) Ion formation from charged droplets—Roles of geometry, energy, and time. *J Am Soc Mass Spectrom* 4:524–535.
6. Kebarle P, Tang L (1993) From ions in solution to ions in the gas-phase—The mechanism of electrospray mass-spectrometry. *Anal Chem* 65:A972–A986.
7. Kebarle P, Peschke M (2000) On the mechanisms by which the charged droplets produced by electrospray lead to gas phase ions. *Anal Chim Acta* 406:11–35.
8. Danckwerts PV, (1970) *Gas–Liquid Reactions* (McGraw–Hill, New York).
9. Enami S, Vecitis CD, Cheng J, Hoffmann MR, Colussi AJ (2007) Global inorganic source of atmospheric bromine *J Phys Chem A* 111:8749–8752.
10. Karagulian F, Lea SA, Dilbeck CW, Finlayson-Pitts BJ (2008) A new mechanism for ozonolysis of unsaturated organics on solids: phosphocholines on NaCl as a model for sea salt particles. *PhysChemChemPhys* 10:528–541.

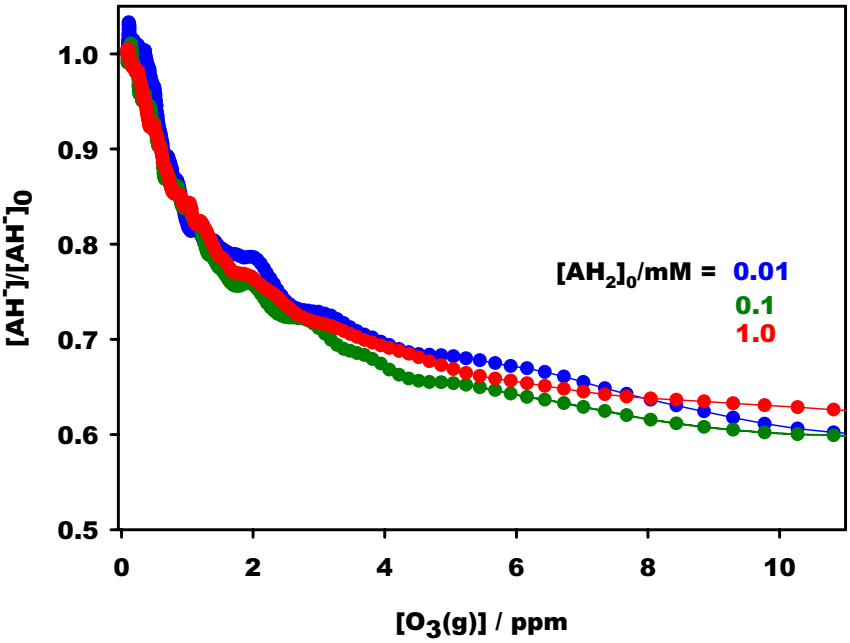

Fig. S1. Lack of initial AH_2 concentration effects on its reactivity toward $O_3(g)$ at pH 3.8.

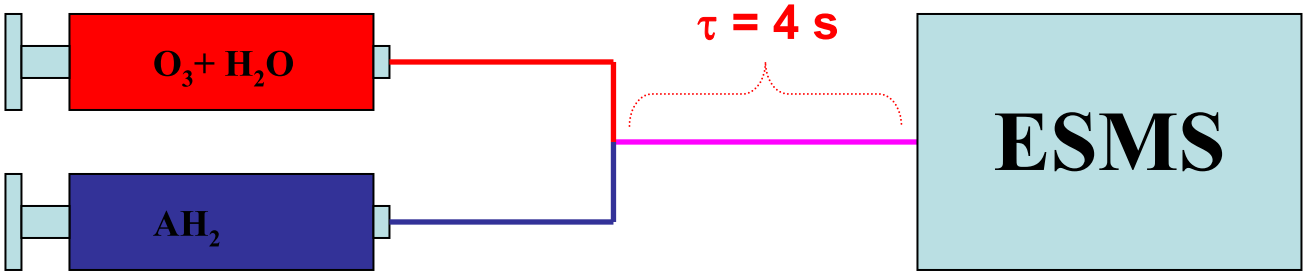

Fig. S2*A*. Continuous flow T-mixer setup used to study the reaction between AH_2 and O_3 in bulk water. Aqueous AH_2 solutions (1 mM) at pH 3.8 and O_3-sparged water were pumped through the T-mixer into the ESMS for analysis after ≈4-s contact time.

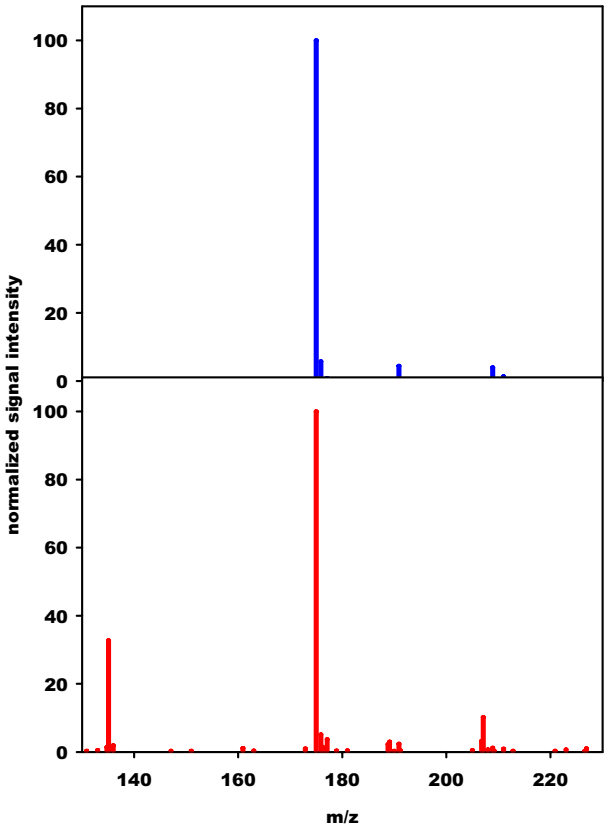

Fig. S2*B*. ESMS of AH_2 in the absence of O_3(aq). ESMS of AH_2 mixed with O_3(aq). Note the formation of THR^- ($m/z = 135$), $DHA{\cdot}H_2O^-$ ($m/z = 191$) and $DHA{\cdot}(H_2O)_2^-$ ($m/z = 209$), and the absence of AOZ^- ($m/z = 223$).

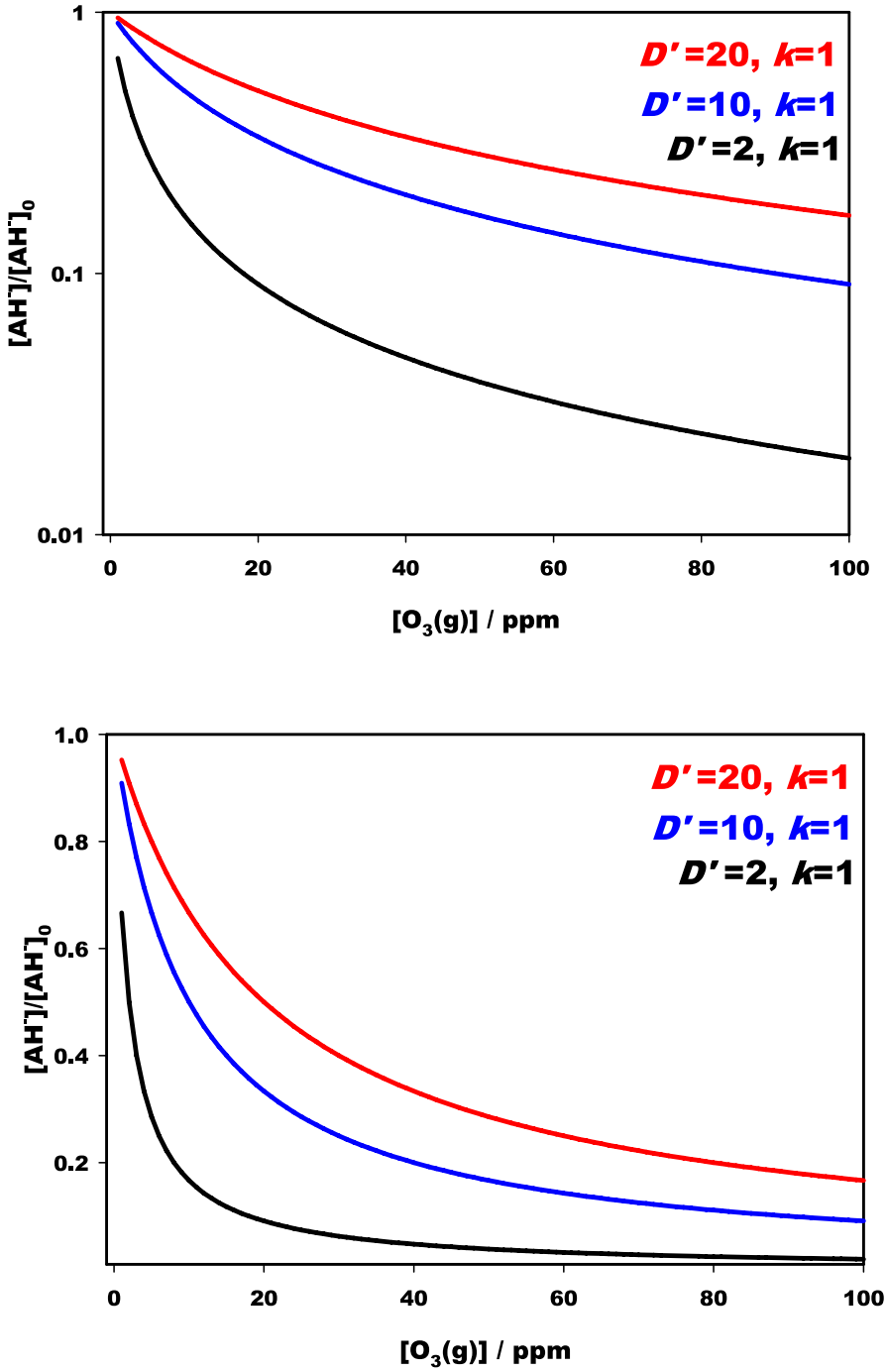

Fig. S3. $[AH^-]/[AH^-]_0$ vs. $[O_3(g)]$ plots calculated from Eq. **3** using the reported parameters. (*Upper*) Log $\{[AH^-]/[AH^-]_0\}$ vs. $[O_3(g)]$. (*Lower*) $[AH^-]/[AH^-]_0$ vs. $[O_3(g)]$.

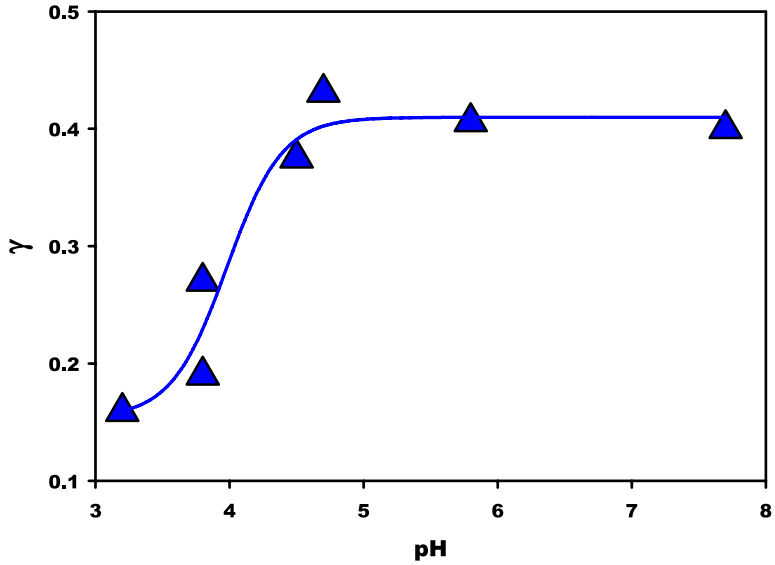

Fig. S4. Symbols indicate initial slopes γ (Eq. **7** and Table S1) vs. bulk pH for the decay of AH^- in the ozonolysis of AH_2. The curve is a best fit to the experimental slopes from Table S1 using the sigmoidal function Eq. **8**. Best-fit parameters lead to $\gamma_{pH>7}/\gamma_{pH<3} = 2.73$. Note that $pH_{0.5} = 3.98 \pm 0.18 \approx pK_{a1}(AH_2) = 4.10$.

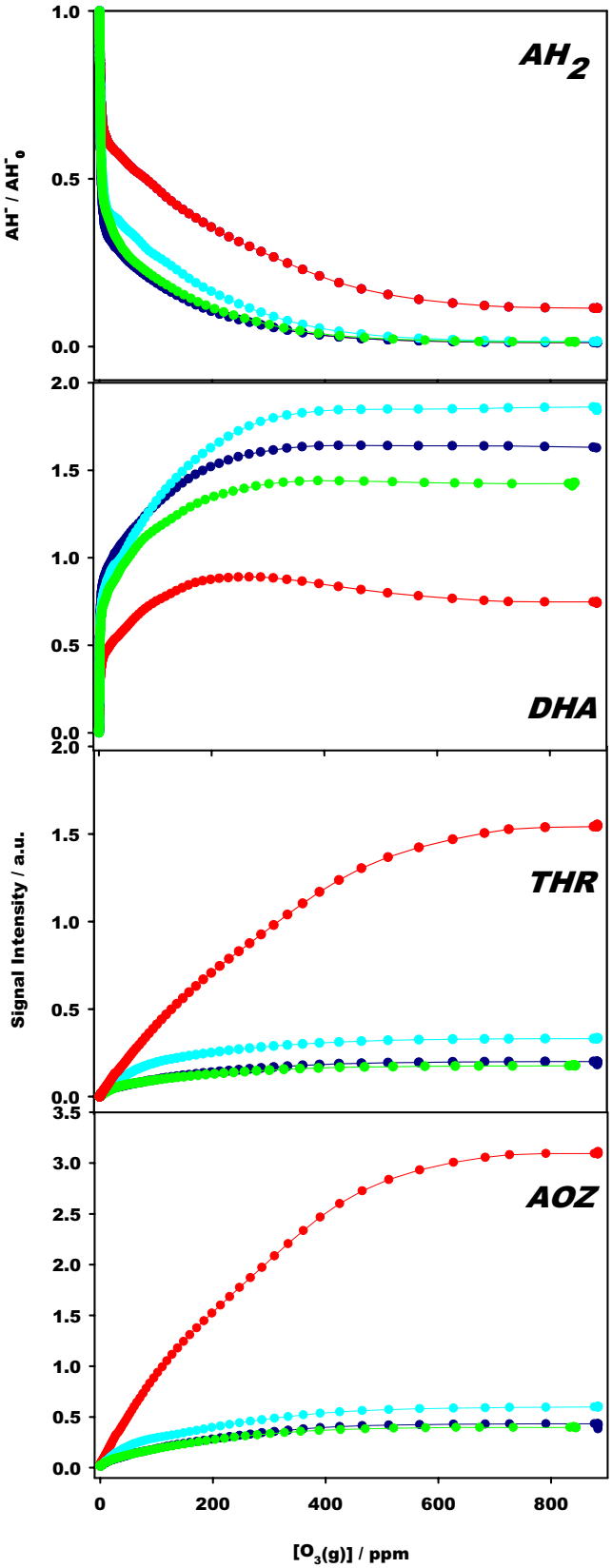

Fig. S5. Ascorbate and reaction products as functions of [O_3(g)] in the range of 0–880 ppm. Red, pH 3.8; light blue, pH 4.7; green, pH 5.8; dark blue, pH 8.1.

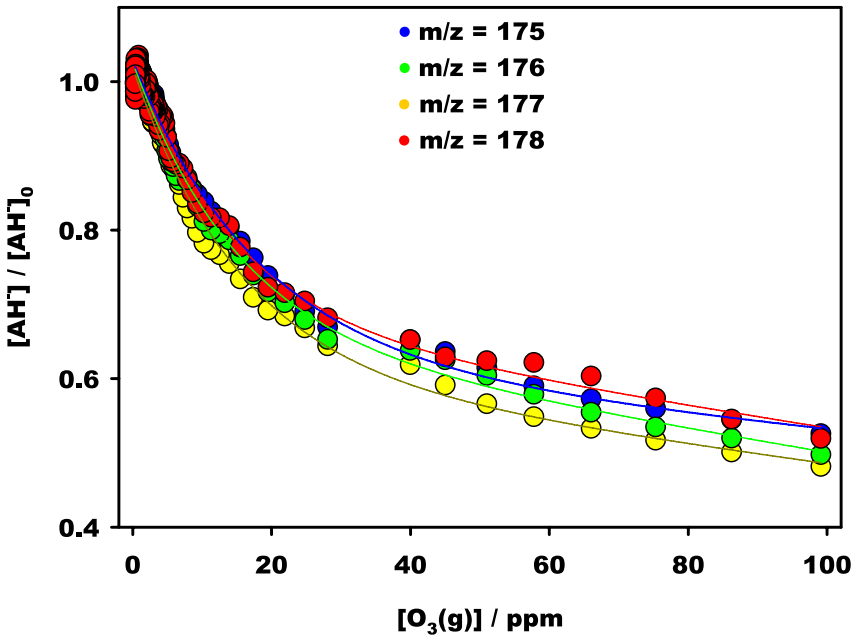

Fig. S6. Decay of OD-substituted AH^- isotopologues as a function of $[O_3(g)]$ in the ozonolysis of 1 mM AH_2 in 50/50 H_2O/D_2O (vol/vol) at pH 6.7. The virtually indistinguishable decays of the various isotopologues exclude significant H-transfer control in the rate-controlling steps of AH_2 ozonolysis.

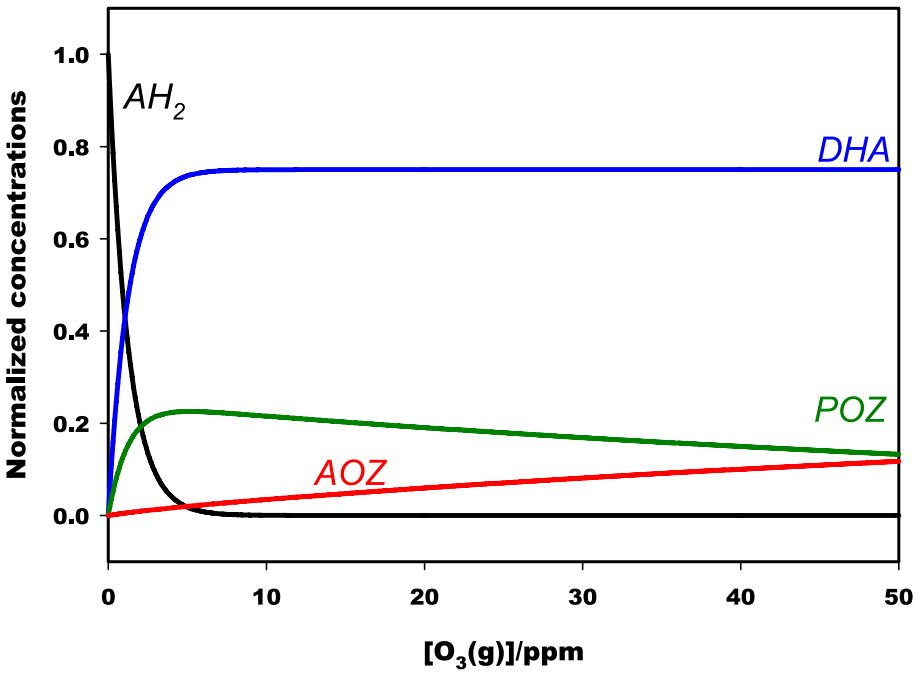

Fig. S7. Results of calculations based on the mechanism and parameters given in *Appendix 4*.

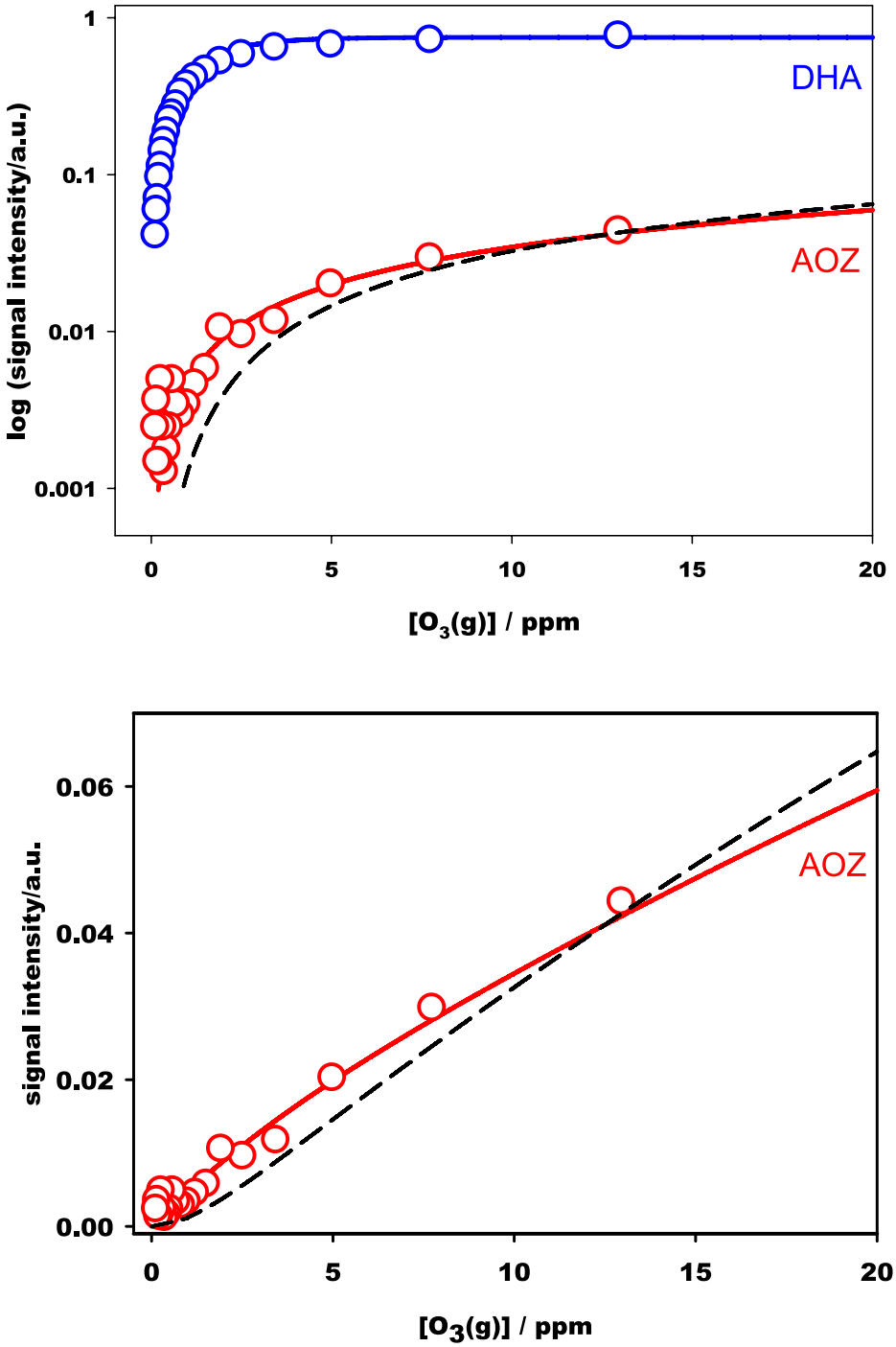

Fig. S8. Symbols indicate experimental data at pH 5.8 from Fig. 3. Solid lines, calculated with the mechanism and parameters given in *Appendix 4*; dashed line, calculated by assuming that the primary ozonide is stable ($k_3 = 0$) but decomposes when assisted by O_3 (9). (*Lower*) Expanded view of the fit to AOZ near the origin in a linear ordinate scale.

Table S1. Parameters obtained by fitting Eq. 5 to the data of Fig. S3 *Upper*

pH	*a*	*b*	*c*	*R**	γ
3.2	0.24 ± 0.00	0.66 ± 0.02	−0.001	0.992	−0.159 ± 0.005
3.8	0.35 ± 0.00	0.53 ± 0.02	−0.0045	0.998	−0.190 ± 0.007
3.8	0.28 ± 0.01	1.18 ± 0.09	−0.0139	0.976	−0.270 ± 0.021
4.5	0.48 ± 0.01	0.76 ± 0.03	−0.0106	0.988	−0.375 ± 0.015
4.7	0.67 ± 0.01	0.63 ± 0.02	−0.009	0.998	−0.431 ± 0.014
5.8	0.70 ± 0.00	0.57 ± 0.01	−0.007	0.999	−0.406 ± 0.007
7.7	0.74 ± 0.01	0.53 ± 0.01	−0.008	0.999	−0.400 ± 0.008

*Correlation coefficient.

Table S2. Initial slopes, γ_P, for the DHA, THR, and AOZ curves of Fig. 3

pH	γ_{DHA}	γ_{THR}	γ_{AOZ}
3.8	755 ± 30	470 ± 2	100.0 ± 0.4
4.7	1896 ± 81	369 ± 5	45.7 ± 0.6
5.8	1572 ± 72	260 ± 3	28.6 ± 0.8
8.1	2577 ± 95	349 ± 5	32.5 ± 1.4